# p115RhoGEF activates RhoA to support tight junction maintenance and remodeling

Shahana A. Chumki[a], Lotte M. van den Goor[b], Benjamin N. Hall[b], and Ann L. Miller[a,b,*]
[a]Cellular and Molecular Biology Graduate Program and [b]Department of Molecular, Cellular, and Developmental Biology, University of Michigan, Ann Arbor, MI 48109

**ABSTRACT** **In vertebrates, epithelial cell–cell junctions must rapidly remodel to maintain barrier function as cells undergo dynamic shape-change events. Consequently, localized leaks sometimes arise within the tight junction (TJ) barrier, which are repaired by short-lived activations of RhoA, called "Rho flares." However, how RhoA is activated at leak sites remains unknown. Here we asked which guanine nucleotide exchange factor (GEF) localizes to TJs to initiate Rho activity at Rho flares. We find that p115RhoGEF locally activates Rho flares at sites of TJ loss. Knockdown of p115RhoGEF leads to diminished Rho flare intensity and impaired TJ remodeling. p115RhoGEF knockdown also decreases junctional active RhoA levels, thus compromising the apical actomyosin array and junctional complex. Furthermore, p115RhoGEF is necessary to promote local leak repair to maintain TJ barrier function. In all, our work demonstrates a central role for p115RhoGEF in activating junctional RhoA to preserve barrier function and direct local TJ remodeling.**

**Monitoring Editor**
Terry Lechler
Duke University

Received: Jun 8, 2022
Revised: Sep 19, 2022
Accepted: Sep 27, 2022

## INTRODUCTION

Epithelial barrier function is critical for tissue development and homeostasis, selectively regulating the movement of molecules and ions across the barrier, while preventing invasion of harmful pathogens (Marchiando *et al.*, 2010). To execute effective barrier function, polarized epithelial cells must establish and maintain adhesion to one another. In vertebrates, cell–cell adhesion is regulated by the apical junctional complex, including tight junctions (TJs) and adherens junctions (AJs) (Hartsock and Nelson, 2008). Transmembrane TJ proteins partner with those in neighboring cells to form branching, strandlike networks that create a selectively permeable barrier (Varadarajan *et al.*, 2019; Saito *et al.*, 2021). Cytoplasmic scaffolding proteins connect TJ strands to an apical array of actomyosin, functionally linking barrier function with cell mechanics (Arnold *et al.*, 2017; Van Itallie *et al.*, 2017).

Dynamic cell shape change events like cell extrusion and cell division challenge cell adhesion and barrier integrity (Guillot and Lecuit, 2013; Gudipaty and Rosenblatt, 2017). When the connection between TJs and the cytoskeleton is compromised, barrier function is disrupted, leading to increased paracellular permeability often correlating with disease states (Zeissig *et al.*, 2007; Ivanov *et al.*, 2010). In response to dynamic cell shape change, TJs actively remodel to maintain their connections and barrier integrity (Rosenblatt *et al.*, 2001; Higashi *et al.*, 2016; Stephenson *et al.*, 2019). However, the mechanisms by which TJs coordinate junction remodeling with cell shape change are not fully understood.

The small GTPase RhoA is a central director of epithelial shape change (Thumkeo *et al.*, 2013; Arnold *et al.*, 2017; Cavanaugh *et al.*, 2020). RhoA acts as a molecular switch, requiring guanine nucleotide exchange factors (GEFs) to promote RhoA's switch from an "inactive" GDP-bound state to an "active" GTP-bound state (Rossman *et al.*, 2005). Spatiotemporally precise activation of Rho to support specific cellular events is often achieved by recruitment and/or activation of

This article was published online ahead of print in MBoC in Press (http://www.molbiolcell.org/cgi/doi/10.1091/mbc.E22-06-0205) on October 6, 2022.

The authors declare no competing financial interests.

Author contributions: S.A.C. and A.L.M. conceptualized the study; S.A.C., L.M.v.d.G., and A.L.M. developed the methodology; S.A.C. performed the majority of experiments and data analysis; L.M.v.d.G. performed experiments for Figure 3 (A, C, F, G) and analyzed data for Supplemental Figure S4A; B.N.H. performed experiments for Supplemental Figure S1B and investigated literature about candidate GEFs; S.A.C., L.M.v.d.G., and A.L.M. wrote the original draft of the manuscript; all authors revised the manuscript; A.L.M. acquired funding; A.L.M. supervised the study.

*Address correspondence to: Ann L. Miller (annlm@umich.edu).

Abbreviations used: AJ, adherens junctions; AUC, area under the curve; CaR, calcium-sensing receptor; FBS, fetal bovine serum; GAP, GTPase-activating protein; GBD, GTPase-binding domain; GEF, guanine nucleotide exchange factor; GPCR, G protein-coupled receptor; HRP, horseradish peroxidase; MMR, Mark's modified Ringers; MO, antisense morpholino oligo; PBS, phosphate-buffered saline; PFA, paraformaldehyde; P-MLC, phospho-myosin II light chain 2; rgRGS, RhoGEF regulator of G-protein signaling; ROI, region of interest; RT, room temperature; TCA, trichloroacetic acid; TJ, tight junctions; ZnUMBA, zinc-based ultrasensitive microscopic barrier assay.

specific RhoGEFs (Garcia-Mata and Burridge, 2007; Fritz and Pertz, 2016). Active RhoA stimulates F-actin assembly and myosin II activation, forming actomyosin contractile arrays that drive a range of cell-scale and tissue-scale contractile events.

In epithelial tissues, active RhoA localizes to apical cell–cell junctions at steady-state tension (Terry *et al.*, 2011; Reyes *et al.*, 2014; Priya *et al.*, 2015). In high-tension environments, such as when acute tensile stress is applied or apoptosis prompts cell extrusion, junctional active RhoA increases to promote downstream actomyosin accumulation that preserves epithelial integrity (Acharya *et al.*, 2018; Duszyc *et al.*, 2021). RhoA also mediates local TJ remodeling in response to leaks in the TJ barrier, which are associated with junction elongation (Stephenson *et al.*, 2019). In response to these barrier breaches, RhoA is activated in transient, local bursts, called "Rho flares" (Stephenson *et al.*, 2019). Rho flares rapidly repair the TJ barrier through localized actomyosin accumulation, which promotes junction contraction and TJ protein reinforcement (Stephenson *et al.*, 2019). Recent work revealed that intracellular calcium flashes, along with the mechanical stimulus of junction elongation, are early events in the Rho flare signaling pathway (Varadarajan *et al.*, 2022). These calcium flashes, mediated through mechanosensitive calcium channels, are required for sustained RhoA activation to support efficient repair and reinforcement of the TJ barrier (Varadarajan *et al.*, 2022). However, a crucial step of the Rho flare TJ remodeling pathway remains unclear: which GEF activates Rho flares?

Here we sought to identify which GEF(s) localize to TJs and directly activate Rho flares. We first investigate the localization of four candidate RhoGEFs. We find that p115RhoGEF localizes to Rho flares during local TJ remodeling. Knockdown of p115RhoGEF decreases Rho flare intensity, leading to impaired TJ remodeling. Furthermore, p115RhoGEF is also required for proper baseline levels of junctional active RhoA, which supports the maintenance of the apical actomyosin array, TJs, and AJs. Finally, we show that p115RhoGEF guards against repeating local barrier leaks and is critical for maintaining TJ barrier function.

## RESULTS

### p115RhoGEF localizes to Rho flares during TJ remodeling

To determine which GEF(s) activate Rho flare-mediated TJ repair, we investigated four candidate GEFs: p115RhoGEF (also known as Arhgef1 or Lsc), LARG (Arhgef12), PDZRhoGEF (Arhgef11), and p114RhoGEF (Arhgef18) using a localization screen in gastrula-stage (Nieuwkoop and Faber stage 10-11) *Xenopus laevis* embryos. These candidates were selected because they possess either an rgRGS (RhoGEF regulator of G-protein signaling) domain known to interact with $G\alpha_{12/13}$ or an alternate domain that interacts with $G\alpha_{12}$ (Fukuhara *et al.*, 2001; Martin *et al.*, 2016). Since *Xenopus* frogs are allotetraploid, we considered gastrula-stage gene expression levels (Session *et al.*, 2016) for each candidate GEF to determine which alloallelle (S vs. L) to investigate (Supplemental Figure S1A). To screen candidate GEFs, embryos were injected with mRNAs encoding the probe for active RhoA (mCherry-2x rhotekin GTPase-binding domain [GBD]; Benink and Bement, 2005; Davenport *et al.*, 2016), fluorescently tagged ZO-1 to mark TJs, and the candidate GEFs C-terminally tagged with mNeon. Live imaging revealed the localization of each of the candidate GEFs relative to Rho flares. PDZRhoGEF.S and p114RhoGEF.S both localized to apical junctions but not at the sites of Rho flares, while LARG.L remained cytosolic (Figure 1A). Notably, we discovered that p115RhoGEF (both p115.S and p115.L) colocalized with active Rho at sites of Rho flares (Figure 1A and Supplemental Figure S1B). Time-lapse imaging demonstrated that weak baseline p115.S signal at apical junctions increased locally at sites of ZO-1 loss, without being depleted from the surrounding junctional regions (Figure 1B, Supplemental Figure S1, C–C′, and Supplemental Video S1). Quantification of multiple movies revealed that the peak intensity of p115.S signal immediately preceded or happened concurrently with the peak of active RhoA, and both quickly returned to baseline as ZO-1 is repaired and reinforced above baseline levels (Figure 1C). Z-depth imaging revealed that p115.S localized at the apical surface of epithelial cells, with p115.S signal partially overlapping with the TJ protein ZO-1 (Supplemental Figure S1, D–D″). Taken together, our data indicate that p115RhoGEF localizes to Rho flares during TJ repair and reinforcement.

### p115RhoGEF is required for Rho flares and local TJ remodeling

To test whether p115RhoGEF is required for local Rho flare activation during TJ remodeling, we decreased p115RhoGEF protein expression using antisense morpholinos oligos (MOs) that block translation of *Xenopus* p115RhoGEF (Supplemental Figure S2, A–D). Initially, we aimed to knock down both the p115.S and the p115.L alloalleles. However, this double p115RhoGEF alloallele knockdown (p115.S+L KD) completely abolished Rho flares (Supplemental Figure S2E), indicating that p115RhoGEF is required for Rho flare initiation, but preventing analysis of Rho flare frequency and behavior. Therefore, going forward, we knocked down a single p115RhoGEF alloallele (p115.S KD), which resulted in detectable Rho flares, which occurred at a higher frequency compared with p115.S+L KD (often at a higher frequency than controls, as well) (Supplemental Figure S2F). Additionally, we used GFP-occludin to detect TJs in these experiments, as ZO-1 signal was quite weak in p115.S KD embryos. Notably, Rho flares in p115.S KD embryos displayed reduced intensity and duration of active RhoA at sites of TJ protein loss (Figure 2, A–C′, and Supplemental Video S2). This reduction in active RhoA at flares led us to test whether downstream TJ repair was also compromised. Indeed, the rapid junction contraction that immediately follows Rho flares in control embryos was absent in p115.S KD embryos (Figure 2, D–D′). We also measured a significant reduction in occludin reinforcement following TJ breaks in p115.S KD embryos compared with controls (Figure 2, B and E–E′). These effects are clearly visualized with kymographs of individual junctions, where controls exhibit robust Rho activation, junction contraction, and occludin reinforcement following TJ damage, whereas p115.S KD embryos exhibit weak, repeating Rho flares that fail to promote junction contraction or occludin reinforcement (Figure 2, F and G; Supplemental Figure S3). We have found that breaks in occludin occur with similar timing to the Rho flare (Stephenson *et al.*, 2019) and correlate with the degree of the membrane protrusion. Due to p115.S KD, the reduced intensity of Rho flares likely produces smaller membrane protrusions and thus smaller occludin breaks. We propose that these weak Rho flares in p115.S KD embryos are below the threshold needed for effective Rho-mediated TJ reinforcement since they frequently repeat along the same junction. Together, these data indicate that p115RhoGEF is required for the initiation and robust local activation of RhoA necessary for effective TJ repair and reinforcement.

### p115RhoGEF is required for junctional RhoA activation to maintain the apical actomyosin array, TJs, and AJs

Knocking down p115RhoGEF revealed a surprising phenotype: compared with controls, p115RhoGEF KD cells displayed a dramatic increase in cell size (Supplemental Figure S4A). Therefore we investigated whether the cell size changes might occur in response to dysfunctional actomyosin contraction at apical cell junctions and/or cytokinesis defects.

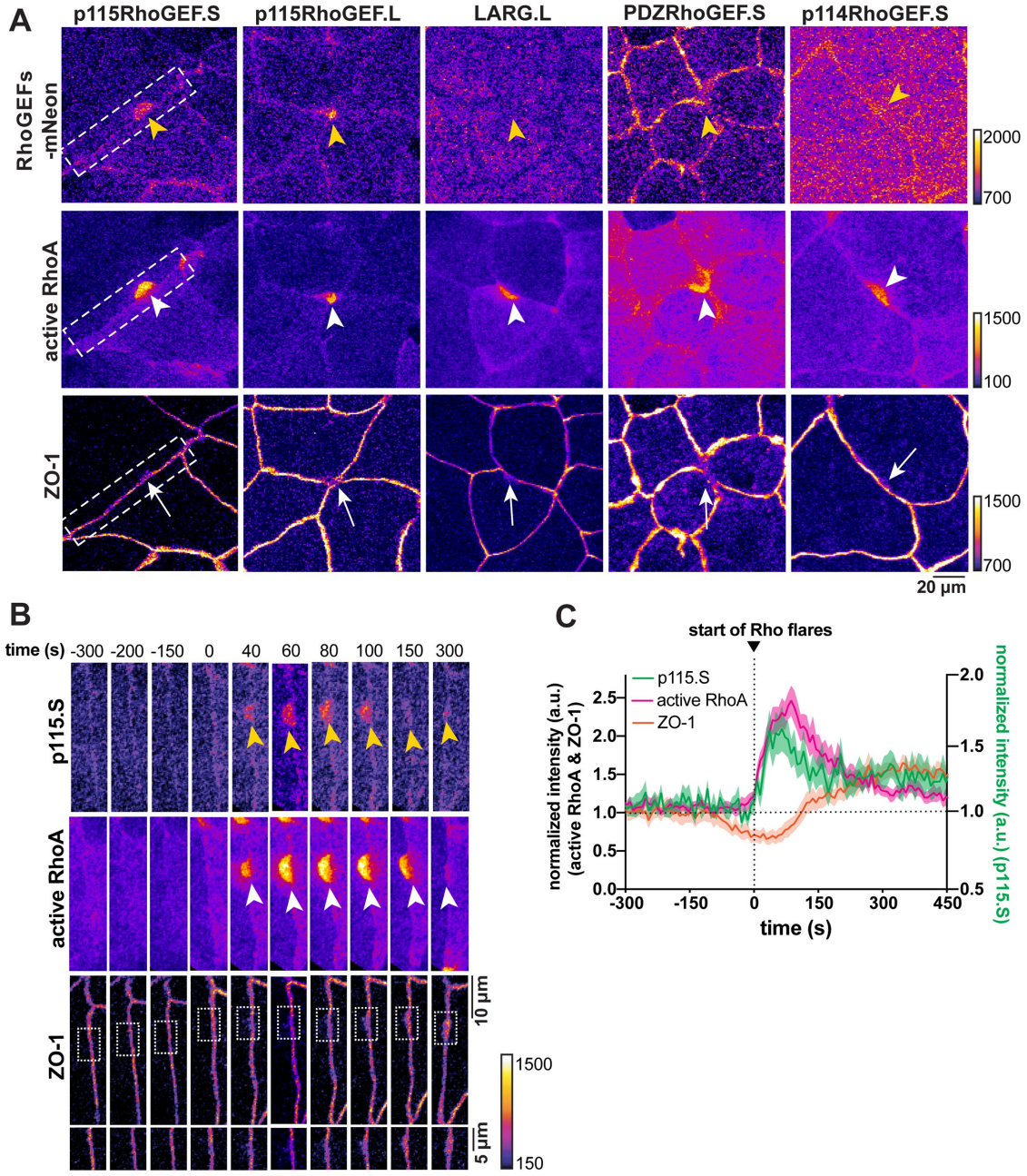


FIGURE 1: p115RhoGEF localizes to Rho flares during TJ remodeling. (A) Cells expressing fluorescently tagged candidate RhoGEFs (p115RhoGEF.S-mNeon, p115RhoGEF.L-mNeon, LARG.L-mNeon, PDZRhoGEF.S-mNeon, and p114RhoGEF.S-mNeon), active RhoA probe (mCherry-2xrGBD), and fluorescently tagged ZO-1 (BFP-ZO-1). All are shown in Fire LUT. The data for each RhoGEF were acquired with the same settings, and the LUTs were adjusted in the same way for each GEF, with the noted differences in LUT scaling for the three different probes. Loss of ZO-1 (white arrows) corresponds to sites of active RhoA flares (white arrowheads). Yellow arrowheads indicate sites of Rho flares in tagged candidate RhoGEF images. (B) Time-lapse montage of junction indicated by the white dashed boxes in A. Local increase in p115.S (yellow arrowheads) occurs at site of ZO-1 loss (white boxed regions enlarged below). p115.S signal intensity peaks with the peak of active RhoA (white arrowheads). Time 0 represents the start of the Rho flare increase. Fire LUT applied to all three probes without enhanced brightness and contrast. (C) Mean normalized intensity of p115.S, active RhoA, and ZO-1 at sites of ZO-1 loss, quantified from B and additional videos; p115.S signal intensity peaks with or slightly before the peak of active RhoA. Shading represents SEM. $n = 15$ flares, 5 embryos, 4 experiments.

We first examined three key proteins that contribute to junction contractility: active RhoA, F-actin, and myosin II. Live imaging revealed a reduction in the baseline levels of active RhoA at apical junctions in p115.S+L and p115.S KD embryos (Figure 3, A and B). Notably, junctional active RhoA intensity was partially rescued when p115.S KD embryos were injected with a p115.S mutant that could not be targeted by the MO (p115.S wobble) (Figure 3, A and B; Supplemental Figure S2A). Additionally, we found that expression of the p115.S wobble mutant partially rescued cell size defects in p115.S KD embryos (Supplemental Figure S4A). Fixed imaging

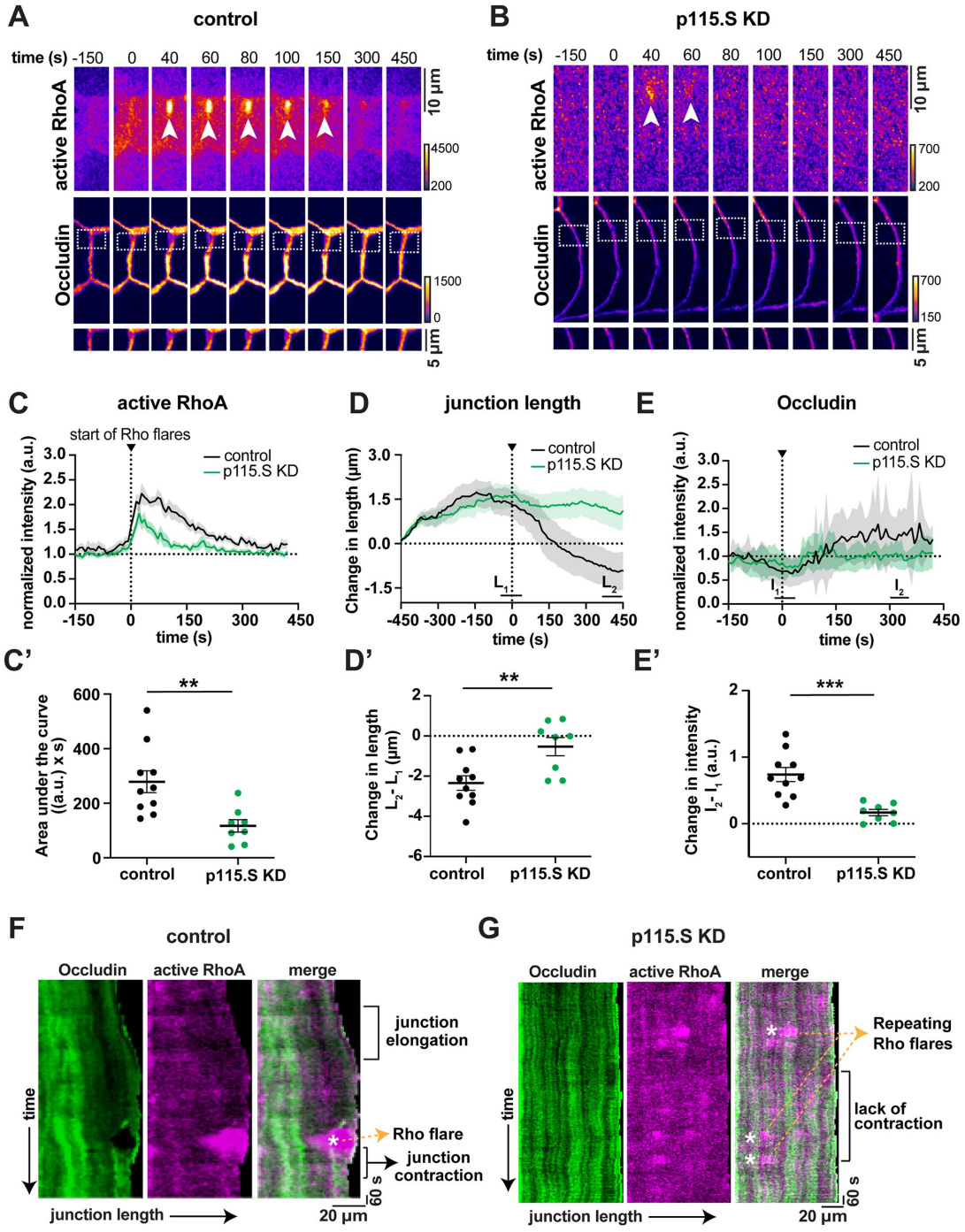


FIGURE 2: p115RhoGEF is required for Rho flares and local TJ remodeling. (A-B) Time-lapse montage of active RhoA (mCherry-2xrGBD, Fire LUT) and GFP-occludin (Fire LUT) in control embryos (A) and p115.S KD embryos (B). p115.S KD flares exhibit decreased Rho activity (white arrowheads) and occludin reinforcement (white dashed boxes, enlarged below) in comparison to controls. Time 0 represents the start of the Rho flare increase. (C-E) Graphs of mean normalized intensity of active RhoA (C), occludin (E), and change in junction length (D) in control (black lines) and p115.S KD Rho flares (green lines) over time. Shading represents SEM. Control: $n = 10$ flares, 3 embryos, 3 experiments; p115.S KD: $n = 8$ flares, 3 embryos, 3 experiments. (C'–E') Scatter plot of AUC for active RhoA (C') was calculated from C; $p = 0.0047$(**). Scatter plot of change in length (D') was calculated from D. $L_1$ and $L_2$ represent average length of junctions from individual traces from time –20–30 s and 400–450 s, respectively; $p = 0.0059$(**). Scatter plot of change in occludin intensity (E') was calculated from E. $I_1$ and $I_2$ represent average intensity of occludin from individual traces from time –20–30 s and 300-350 s, respectively; $p = 0.0004$(***). Error bars represent mean ± SEM; significance was calculated using unpaired *t* tests. (F–G) Kymographs of occludin (green), active RhoA (magenta), and merged image from representative junctions projected from vertex-to-vertex over time in control (F) and p115.S KD (G) embryos. Kymographs highlight repeated Rho flares, lack of occludin reinforcement, and lack of junction contraction in p115.S KD embryos (note that p115.S KD kymographs were enhanced for brightness and contrast, as p115RhoGEF KD reduces signal intensity of occludin and active RhoA [see Supplemental Figure S3 for raw data]).

revealed significantly decreased F-actin (phalloidin) and phosphomyosin II light chain 2 (P-MLC) intensity at apical junctions in p115RhoGEF KD embryos, which was rescued by expression of p115.S wobble (Figure 3, C–E).

Since cytoskeletal rearrangements are crucial for cell migration and intercalation during morphogenesis (Huebner and Wallingford, 2019), we predicted that this loss of actomyosin junction contractility due to p115RhoGEF KD could cause developmental defects during morphogenesis. Indeed, p115.S+L KD embryos did not progress past gastrulation (Supplemental Figure S4B). The p115.S KD embryos exhibited severe delays in body axis elongation that were partially rescued with p115.S wobble expression (Supplemental Figure S4B).

Given that disruptions in actomyosin contractility are correlated with dysfunctional cell–cell junction complexes (Turner, 2000; Arnold *et al.*, 2017), we next asked if TJs and AJs are compromised in p115RhoGEF KD embryos. Previous work had reported that depletion of p115RhoGEF in breast cancer epithelial cell lines leads to a reduction in the AJ protein E-cadherin along with enhanced cell protrusion and migration (Kher *et al.*, 2014). Immunofluorescence imaging of *Xenopus* embryos demonstrated that both TJ (ZO-1) and AJ (E-cadherin) proteins were significantly reduced at junctions upon p115RhoGEF KD (Figure 3, F–H). Interestingly, enlarged images of ZO-1 in p115RhoGEF KD embryos reveal a discontinuous signal compared with controls (Figure 3F). This effect was also observed by live imaging of BFP-ZO-1; the ZO-1 signal in p115.S+L KD cells was patchy and discontinuous, whereas the ZO-1 signal in control cells was continuous (Supplemental Figure S5). Despite careful handling of trichloroacetic acid (TCA)-fixed embryos, we noted the presence of "cracks" between TJs in p115RhoGEF KD embryos (Figure 3F); although we believe this is a fixation artifact because it was not detected in live imaging (Supplemental Figure S5), it suggests that p115RhoGEF KD embryos are more susceptible to damage. Importantly, expression of the p115.S wobble mutant in p115.S KD embryos restores ZO-1 and partially restores E-cadherin to intensities similar to those measured in control embryos (Figure 3H). Additionally, p115.S wobble expression rescues the discontinuous ZO-1 signal and the "cracks" between TJs (Figure 3F).

Our data reveal that p115RhoGEF is necessary for junctional RhoA activation to maintain the apical actomyosin array, TJs and AJs and disruption of Rho-mediated contractility at apical cell–cell junctions may contribute to the larger cell size in p115RhoGEF KD embryos. We also investigated whether cytokinesis defects could underlie the cell size increase. We did not capture evidence of failed cell division, such as failed cytokinetic furrow ingression, during live imaging of p115.S KD cells (Supplemental Figure S6A). However, imaging with a nuclear marker (mCherry-H2B) did reveal larger nuclei and multinucleate cells in p115RhoGEF KD embryos when compared with controls (Supplemental Figure S6B), so the possibility that p115RhoGEF can contribute to regulating cytokinesis in epithelial tissues should be further examined in future studies. Due to their multinucleation and larger size, the p115RhoGEF KD cells may be mechanically altered. Of note, we have previously demonstrated that perturbing MgcRacGAP, which disrupts cytokinesis and leads to larger cells, does not result in discontinuous TJ signal (Breznau *et al.*, 2015). This suggests that the effect we see on TJs (Figures 3F and H) is specific to p115RhoGEF and is not simply due to the enlarged cell size. Collectively, these findings demonstrate that p115RhoGEF is required for junctional active RhoA to support the maintenance of the apical actomyosin array, TJs, and AJs in vertebrate epithelial tissue.

### p115RhoGEF prevents repeated local leaks to maintain TJ barrier function

Since p115RhoGEF knockdown leads to compromised local TJ remodeling and disrupted maintenance of the apical junctional complex (Figures 2 and 3), we next investigated if p115RhoGEF is required for epithelial barrier function. To assay barrier function, we performed zinc-based ultrasensitive microscopic barrier assay (ZnUMBA [Stephenson *et al.*, 2019]) to detect transient, local TJ leaks. Briefly, this assay utilizes the fluorogenic dye FluoZin-3, which increases in intensity significantly when it encounters zinc ions. *Xenopus* embryos are injected with FluoZin-3 in the blastocoel cavity and mounted in media containing $ZnCl_2$. When the barrier is intact, FluoZin-3 signal remains low and stable, but when the barrier is breached, bright FluoZin-3 signal is detected at the site of barrier damage. We found that whole-field fluorescence intensity of FluoZin-3 signal rapidly increased over time in p115RhoGEF KD embryos compared with controls (Figure 4, A and B), indicating a defect in barrier function when p115RhoGEF is knocked down. When we examined individual junctions, we detected repeated local leaks in p115.S KD embryos that were not efficiently repaired by the Rho flare pathway. Kymographs of individual p115.S KD junctions demonstrated local barrier leaks, as evidenced by increased FluoZin-3 signal, that occurred repeatedly but were not followed by occludin reinforcement (Figure 4D). In contrast, FluoZin-3 leaks in control embryos were rapidly resolved upon junction contraction, and the TJ was reinforced (Figure 4C). Thus, we conclude that p115RhoGEF is required to promote local repair and reinforcement of TJ leaks in order to maintain barrier function, and we propose that the overall weakening of AJs and TJs upon p115RhoGEF KD could make junctions more susceptible to local leaks.

## DISCUSSION

In this study, we identified *Xenopus* p115RhoGEF as a RhoGEF that activates RhoA to support TJ maintenance and local TJ remodeling (Figure 5). p115RhoGEF accumulates at local sites of TJ loss, and it is required for Rho flare activation, which leads to efficient junction contraction and TJ reinforcement. Furthermore, p115RhoGEF KD compromises junction maintenance, causing decreased junctional active RhoA, reduced apical actomyosin, discontinuous TJs, and reduced AJs. The functional consequence of p115RhoGEF KD is defective barrier function due to repeated local leaks in the TJ barrier. To our knowledge, the local recruitment p115RhoGEF to leak sites is the first demonstration of p115RhoGEF's ability to regulate subcellular RhoA activation on a rapid timescale.

Given the necessity of p115RhoGEF for Rho flare activation (Figure 2), it is logical to consider how this GEF coordinates with other early events in Rho flare-mediated TJ remodeling, including junction elongation and cytoplasmic calcium flashes. We previously reported that the mechanical stimulus of junction elongation induces Rho flares and activates mechanosensitive calcium channel-dependent calcium influx (Varadarajan *et al.*, 2022). In fibroblasts, p115RhoGEF, along with fellow rgRGS GEF LARG, is known to activate RhoA following adhesion to fibronectin (Dubash *et al.*, 2007). This activation of p115RhoGEF, which happens at sites where actomyosin stress fibers insert into focal adhesions that mechanically link the cell to the extracellular matrix, may be mechanosensitive. Furthermore, in endothelial cells, tension imposed on junctional adhesion molecule A (JAM-A) activates RhoA, which leads to increased cell stiffness through kinase-mediated activation of p115RhoGEF and GEF-H1 (Scott *et al.*, 2016). Our study now reveals that p115RhoGEF can be recruited and activated upon changes in local

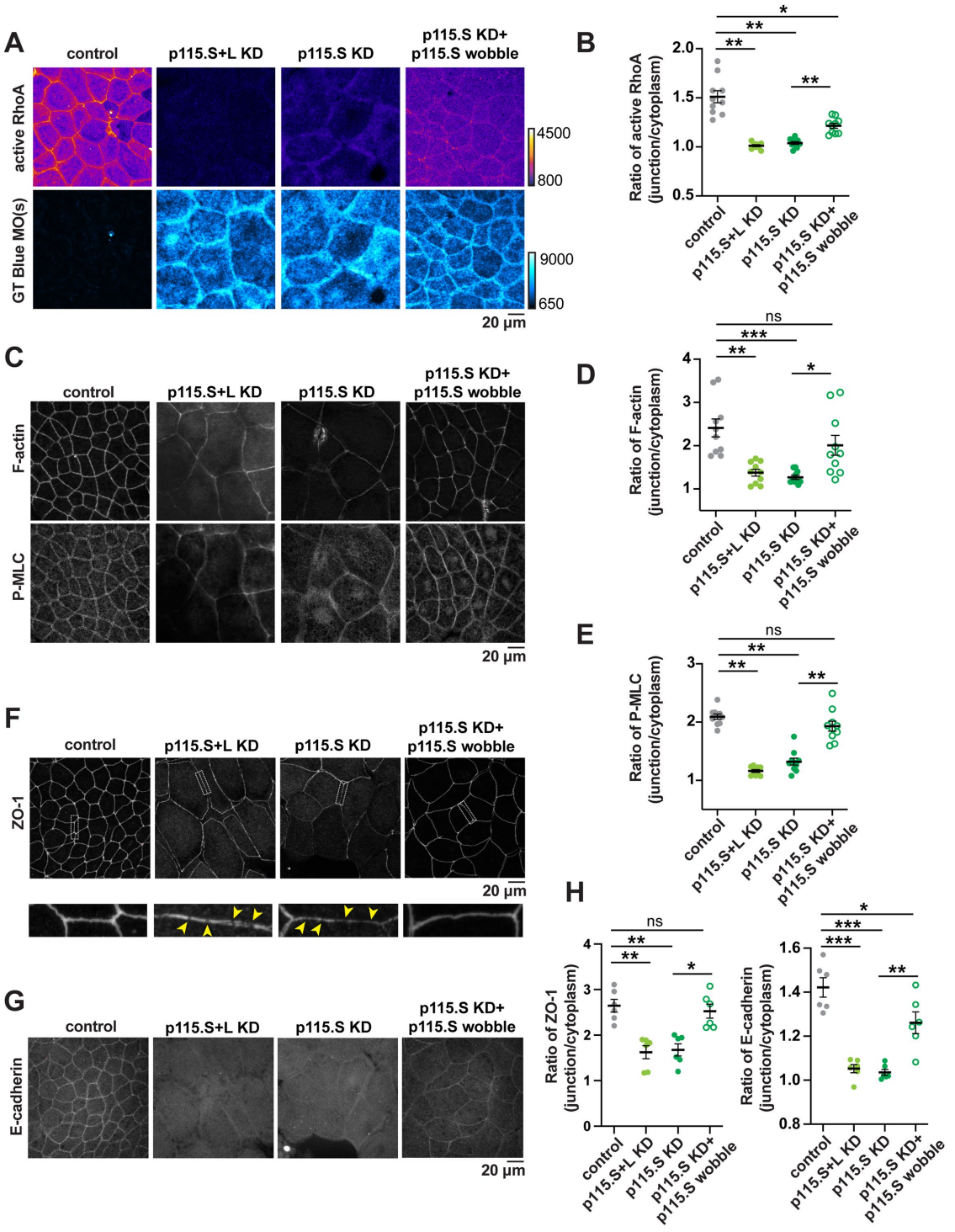


FIGURE 3: p115RhoGEF is required for junctional RhoA activation to maintain the apical actomyosin array, TJs, and AJs. (A-B) Live imaging of cells expressing active RhoA probe (mCherry-2xrGBD, Fire LUT) in control, p115.S+L KD, p115.S KD, and p115.S KD + p115.S wobble embryos. The data for each condition was acquired with the same settings, and the LUTs were adjusted in the same way for each. GeneTools-Blue MO(s), when present, are shown in blue (Cyan Hot LUT). (B) Ratio of junction/cytoplasm signal of RhoA is reduced with p115RhoGEF KD. Injection of p115.S wobble partially rescues junctional active RhoA intensity. $p = <0.0001$(**) and $p = 0.003$(*). Error bars represent mean ± SEM; significance was calculated using unpaired *t* tests. Control: $n = 10$ embryos, 3 experiments; p115.S+L KD: $n = 10$ embryos, 3 experiments; p115.S KD: $n = 10$ embryos, 3 experiments; p115.S KD + p115.S wobble: $n = 10$ embryos, 3 experiments. (C–E) (C) Sum projection of fixed staining for F-actin (Alexa Fluor 488 or 647 phalloidin), P-MLC (anti-P-MLC) in control, p115.S+L KD, p115.S KD, and p115.S KD + p115.S wobble embryos. (D) Ratio of junction/cytoplasm signal of F-actin is reduced with p115RhoGEF KD and rescued with p115.S wobble injection. $p = <0.0001$(***), $p = 0.0002$(**), and $p = 0.0055$(*). (E) Ratio of junction/cytoplasm signal of P-MLC is reduced with p115RhoGEF KD and rescued with p115.S wobble injection. $p = <0.0001$(**). Error bars represent mean ± SEM; significance was calculated

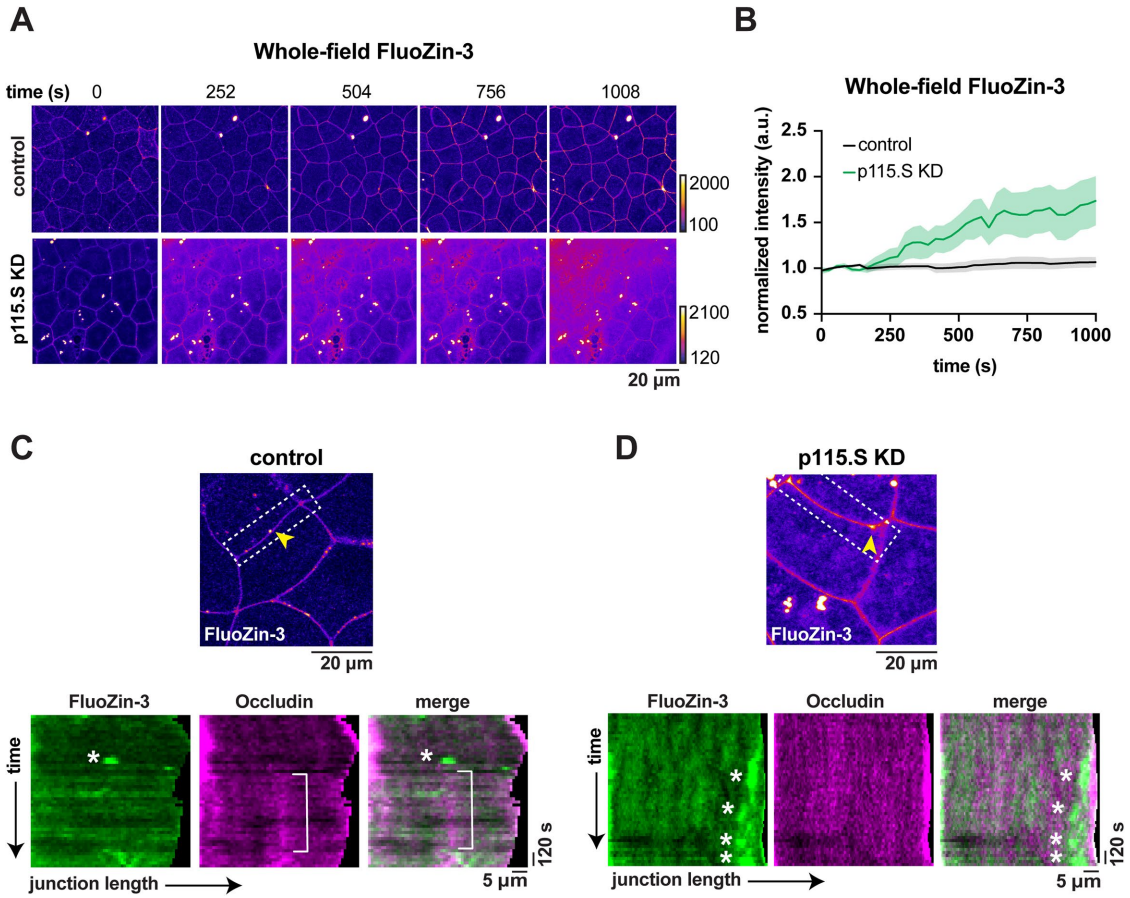


FIGURE 4: p115RhoGEF prevents repeated local leaks to maintain TJ barrier function. (A) Time-lapse images (Fire LUT) of whole-field epithelial barrier permeability determined using ZnUMBA (FluoZin-3 intensity) in control and p115.S KD embryos. Time 0 represents mounting of embryos in 1 mM Zinc-chloride in 0.1 × MMR and the start of the time-lapse movie. (B) Graph of mean normalized intensity of whole-field FluoZin-3 signal intensity in control (black line) and p115.S KD (green line) embryos. Whole-field FluoZin-3 signal increases rapidly over time upon p115.S KD in comparison to control. Shading represents SEM. Control: $n = 5$ embryos, 3 experiments; p115.S KD: $n = 5$ embryos, 3 experiments. (C, D) Cell view of FluoZin-3 signal in control (C) and p115.S KD (D) embryos. White dashed rectangles represent the junctions used to make the kymographs. Kymographs of FluoZin-3 (green), occludin (mCherry-occludin, magenta), and merged image projected from vertex-to-vertex over time in control and p115.S KD embryos. Control embryos display one prominent FluoZin-3 leak (asterisk) and occludin reinforcement (white bracket). Repeated local barrier leaks (white asterisks) and lack of occludin reinforcement occur in p115.S KD embryos.

junction tension at sites of TJ damage. It will be of interest to further investigate mechanisms that may mediate recruitment and activation of p115RhoGEF at epithelial cell–cell junctions in a tension-dependent manner.

Another open question is how p115RhoGEF recruitment and activation coordinates with the local mechanosensitive calcium flashes that precede Rho flare activation (Varadarajan *et al.*, 2022). There is evidence that protein kinase C-α (PKC-α), a kinase regulated by calcium, phosphorylates p115RhoGEF, enhancing RhoA-mediated actomyosin rearrangements in endothelial cells (Holinstat *et al.*, 2003). Furthermore, depletion of the calcium-sensing receptor (CaR), a member of the G protein-coupled receptor (GPCR) superfamily, and/or p115RhoGEF in prostate cancer cell lines reduces aberrantly high levels of calcium-mediated choline kinase signaling, resulting

using unpaired *t* tests. Control: $n = 10$ embryos, 3 experiments; p115.S+L KD: $n = 10$ embryos, 3 experiments; p115.S KD: $n = 10$ embryos, 3 experiments; p115.S KD + p115.S wobble: $n = 10$ embryos, 3 experiments. (F) Sum projection of fixed staining for TJs (anti-ZO-1) in control, p115.S+L KD, p115.S KD, and p115.S KD + p115.S wobble embryos. White dashed rectangle of individual junctions is enlarged below; yellow arrowheads indicate discontinuities in ZO-1 signal. (G) Sum projection of fixed staining for AJs (anti-E-cadherin) in control, p115.S+L KD, p115.S KD, and p115.S KD + p115.S wobble embryos. (H) Ratio of junction/cytoplasm signal of ZO-1 and E-cadherin is reduced with p115RhoGEF KD. Injection of p115.S wobble rescues ZO-1 and E-cadherin signal. For ZO-1 graph: $p = 0.0005$(**) and $p = 0.0019$(*). For E-cadherin graph: $p = <0.0001$(***), $p = 0.0013$(**), and $p = 0.0349$(*). Error bars represent mean ± SEM; significance was calculated using unpaired *t* tests. Control: $n = 6$ embryos, 2 experiments; p115.S+L KD: $n = 6$ embryos, 2 experiments; p115.S KD: $n = 6$ embryos, 2 experiments; p115.S KD + p115.S wobble: $n = 6$ embryos, 2 experiments.

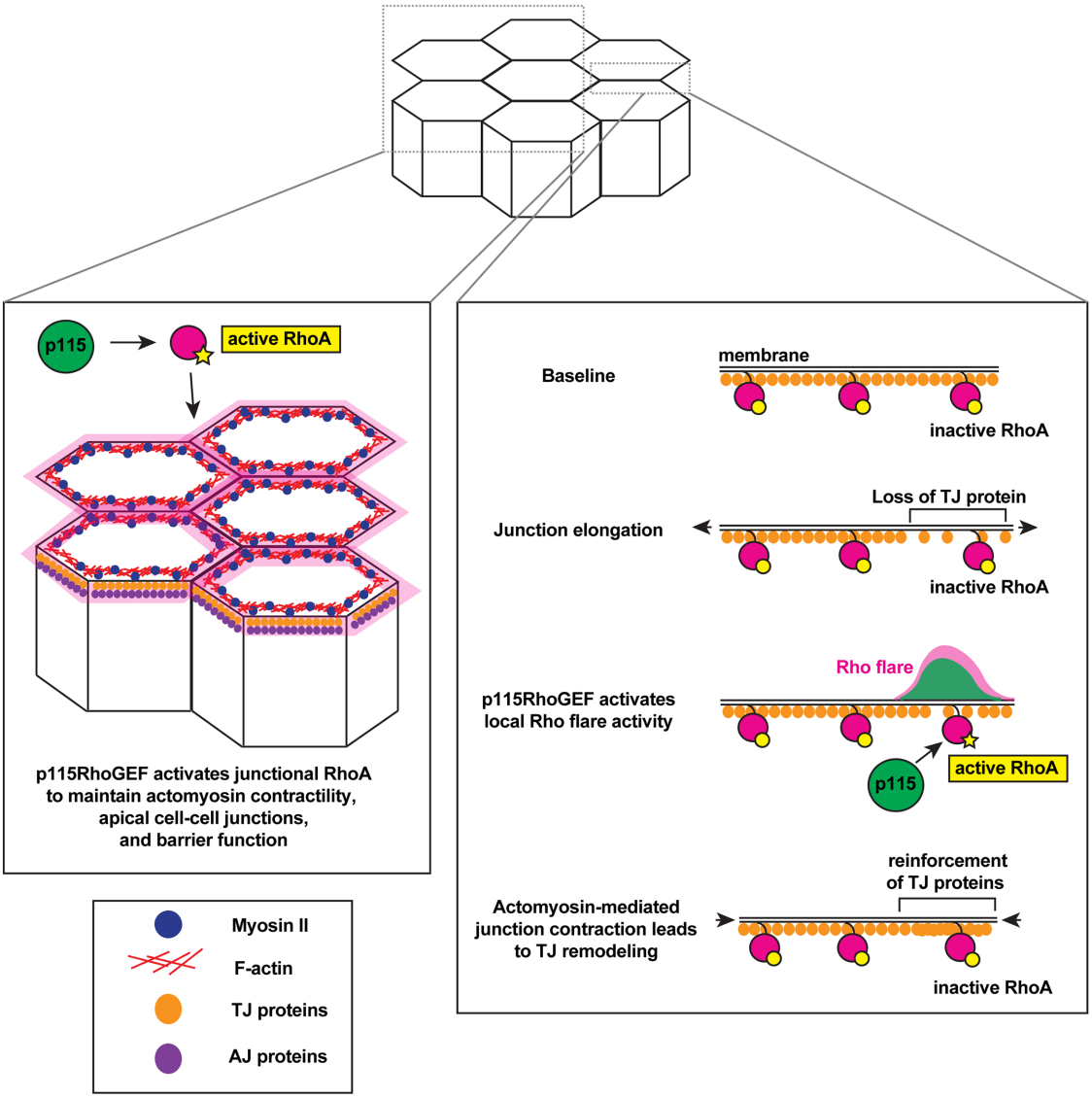


FIGURE 5: The role of p115RhoGEF in TJ maintenance and local TJ remodeling. Model showing mechanism by which p115RhoGEF activates RhoA for TJ maintenance and local remodeling. Top: 3D view of epithelial cells. Bottom left: 3D view of cell–cell junctions showing that p115RhoGEF maintains baseline junctional RhoA activation to support the actomyosin array, TJs, and AJs. Bottom right: en face view of junction highlighted showing how p115RhoGEF recruitment and/or activation at sites of TJ damage activates Rho flares for local TJ repair and remodeling.

in decreased tumor cell proliferation (Huang *et al.*, 2011). Notably, the CaR GPCR couples to large G proteins, including $G\alpha_{12/13}$. As an rgRGS protein, p115RhoGEF can be activated by $G\alpha_{12/13}$, and p115RhoGEF also acts as a GTPase-activating protein (GAP) toward $G\alpha_{12/13}$ (Kozasa *et al.*, 1998). Alternatively, there could be other tension-mediated pathways that activate p115RhoGEF via adhesion GPCRs signaling through $G\alpha_{12/13}$ (Storch *et al.*, 2012; Vizurraga *et al.*, 2020). Collectively, these studies support the notion that calcium signaling may modulate p115RhoGEF activity to ensure robust RhoA activation at sites of local barrier leaks. Future studies should investigate the molecular connection between mechanosensitive calcium signaling and p115RhoGEF recruitment and activation during the Rho flare TJ repair pathway.

In addition to the new role we report for p115RhoGEF in regulating TJ remodeling in response to local leaks in the barrier, our work also reveals that p115RhoGEF is required to maintain baseline junctional active RhoA levels to uphold the apical junctional complex and actomyosin array (Figure 3). Previous experiments in breast cancer epithelial cell lines demonstrated that loss of p115RhoGEF reduces junctional E-cadherin (Kher *et al.*, 2014), consistent with our results in p115RhoGEF KD *Xenopus* embryos (Figure 3). The previous study did not detect continuous ZO-1 signal—even in control cells—so it is hard to determine if p115RhoGEF depletion affected TJ organization (Kher *et al.*, 2014). However, in *Xenopus* embryos, p115RhoGEF KD cells displayed discontinuous ZO-1 signal compared with continuous ZO-1 signal in controls as detected by both immunofluorescence and live imaging (Figure 3 and Supplemental Figure S5). Additionally, in this study, we provide new functional data using our sensitive live imaging barrier assay indicating that there are repeating local barrier leaks in p115RhoGEF KD embryos. Together, our data show that p115RhoGEF regulates barrier function by locally activating Rho to repair local barrier leaks that happen when cells change shape. It is advantageous that p115RhoGEF is recruited specifically to the site of TJ damage to locally activate Rho

to reinforce TJs, as increasing Rho activity globally at apical junctions would likely break down junctions rather than repair them.

We noted that p115RhoGEF KD cells are significantly larger than control cells (Supplemental Figure S4). Interestingly, it appears that p115RhoGEF depletion also led to increased cell size in breast cancer epithelial cell lines (Kher *et al*., 2014). Though live imaging documented p115.S KD cells in gastrula-stage *Xenopus* embryos successfully undergoing cytokinesis (Supplemental Figure S6A), we did find evidence of multinucleate cells in p115RhoGEF KD embryos (Supplemental Figure S6B), suggesting that loss of p115RhoGEF may lead to cytokinesis defects in epithelial tissue. p115RhoGEF has not been reported as a RhoGEF that regulates cytokinesis in isolated cells. Instead, other RhoGEFs, such as Ect2 and GEF-H1, coordinate localized RhoA activation at the cell equator by interacting with the Centralspindlin complex on the plus ends of microtubules (Ect2) or by activation via release from depolymerizing microtubules (GEF-H1) (Yuce *et al*., 2005; Birkenfeld *et al*., 2007). It would be interesting if p115RhoGEF has a role in cytokinesis that only becomes evident in tissues, where the dividing cell needs to maintain and remodel its cell–cell junctions with its neighboring cells while pinching in two. Vinculin is recruited to sites where the contractile ring in the dividing cell is pulling on the junction with its neighboring cell in order to strengthen the connection of the AJ to the actin cytoskeleton (Higashi *et al*., 2016). It is possible that other proteins are also mechanosensitively recruited to these sites. Alternatively, reduced junctional actomyosin in p115RhoGEF KD cells could contribute to reduced tissue stiffness, a factor that also influences cell division (Moruzzi *et al*., 2021). Future work will be needed to determine how p115RhoGEF contributes to successful cytokinesis in epithelial tissues.

Our study demonstrates that p115RhoGEF is important for maintaining apical cell–cell junctions (Figure 3). Other RhoGEFs have also been implicated in TJ formation and maintenance (Citi *et al*., 2011; Arnold *et al*., 2019). Our candidate rgRGS GEF screen revealed that like p115RhoGEF, both PDZRhoGEF and p114RhoGEF localize at apical cell–cell junctions in gastrula-stage *Xenopus* embryos; however, these two RhoGEFs were not enriched at sites of ZO-1 loss (Figure 1). How does p115RhoGEF collaborate with other GEFs to regulate junction formation and maintenance? p114RhoGEF is crucial for TJ formation and protects AJs against acute tensile stress (Terry *et al*., 2011; Acharya *et al*., 2018). It is possible that there is a temporal shift in which RhoGEF is the primary junctional RhoA regulator (e.g., a handoff from p114RhoGEF to p115RhoGEF after TJs are established). Another possibility is a spatial separation of their activities. For example, p115RhoGEF and p114RhoGEF orthologs are spatially separated during morphogenesis in the *Drosophila* ectoderm; dRhoGEF2 (ortholog of p115RhoGEF) activates Rho1 at the medial-apical surface of cells, whereas dp114RhoGEF activates Rho1 at AJs (Garcia De Las Bayonas *et al*., 2019). GEF-H1 associates with TJs and microtubules in MDCK epithelial cells and is required for selective permeability at TJs (Benais-Pont *et al*., 2003). It is possible that GEF-H1 exerts its role as a junctional RhoGEF under conditions where it is activated by phosphorylation or release from microtubules. Here we demonstrated that p115RhoGEF regulates barrier function in *Xenopus* epithelial cells, as knockdown of p115RhoGEF compromises barrier function and disrupts repair of local leaks (Figure 4). Our findings highlight the importance of p115RhoGEF in activating RhoA to promote TJ maintenance and remodeling. In future studies, it will be of high interest to continue to define how p115RhoGEF and other RhoGEFs cooperate to regulate active Rho dynamics at cell–cell junctions.

## MATERIALS AND METHODS

Request a protocol through *Bio-protocol*.

### DNA constructs and p115RhoGEF morpholinos

*Xenopus* rgRGS GEF sequences were synthesized by Twist Biosciences. p115RhoGEF.S (NCBI XR_001932480.2) and p115RhoGEF.L (NCBI XM_041569534.1) were ligated into the *EcoRI* and *XhoI* sites of pCS2+/C-mNeon. p115.S wobble was generated using a gBlock from Integrated DNA Technologies and cloned into the *EcoRI* and *SphI* sites of pCS2+/p115.S-mNeon to make pCS2+/p115.S wobble-mNeon. To make an untagged construct, p115.S-wobble sequence was later cloned into the *XbaI* and *XhoI* sites of pCS2+. LARG.L (NCBI XM_018225772.2) and PDZRhoGEF.S (NCBI XM_018233487.2) were ligated into the *BamHI* and *ClaI* sites of pCS2+/C-mNeon. p114RhoGEF.S (NCBI XM_018243648.2) was ligated into the *XhoI* and *XbaI* sites of pCS2+/C-mNeon. pCS2+/GFP-occludin was generated by amplifying *X. laevis* occludin from a cDNA clone purchased from Thermo Fisher (Clone ID: 7009477) and was ligated into the *BglII* and *EcoRI* sites of pCS2+/N-GFP. All constructs were verified by sequencing. The following constructs were previously described: pCS2+/mCherry-2xrGBD (probe for active Rho; Davenport *et al*., 2016), pCS2+/BFP-ZO-1 and pCS2+/mCherry-occludin (Stephenson *et al*., 2019), and pCS2+/mCherry-H2B (Higashi *et al*., 2016).

The p115RhoGEF antisense morpholinos (MOs) (GeneTools) were designed to target the end of the 5′UTR and start of the coding region of p115.S (MO sequence: CCAAAUUCGUCCAGAUCCAUCUC) or p115.L (MO sequence: CCAUCGUCUGAAUCCAUCUCCUG). A second p115.S MO (MO sequence: CCAAAUUCGUCCAGAUCCAUCUC) was tagged with a 3′-Gene Tools Blue fluorophore (referred to as GT Blue-MO in figures) to visualize which cells contain the MO using live or fixed imaging.

### mRNA preparation

Plasmid DNAs were linearized with *NotI*, except for BFP-ZO-1 and PDZRhoGEF.S, which were linearized with *KpnI*. In vitro mRNA transcription was performed from linearized plasmids using the mMessage mMachine SP6 Transcription Kit (Fisher, #AM1340) and purified using the RNeasy Mini Kit (Qiagen, #74104). RNA transcript sizes were confirmed using 1% agarose gels containing 0.05% bleach and Millennium RNA markers (Fisher, #AM7150).

### *Xenopus* embryos and microinjections

All studies conducted using *X. laevis* embryos strictly adhered to the compliance standards of the U.S. Department of Health and Human Services *Guide for the Care and Use of Laboratory Animals* and were approved by the University of Michigan Institutional Animal Care and Use Committee. *Xenopus* eggs were collected, in vitro fertilized, and dejellied using methods described previously (Miller and Bement, 2009; Woolner *et al*., 2009). Embryos were stored in 0.1× Mark's modified Ringer's (MMR) containing 10 mM NaCl, 0.2 mM KCl, 0.2 mM $CaCl_2$, 0.1 mM $MgCl_2$, and 0.5 mM HEPES, pH 7.4, at 15°C to prolong the two-cell and four-cell stages for microinjection. Embryos were microinjected as previously described (Reyes *et al*., 2014). For p115RhoGEF knockdown and replacement experiments, all four cells at the four-cell stage were first injected with either 10 nL of a mixture of p115.S and p115.L MOs (2 mM needle concentration each) or 5 nL of p115.S MO (2 mM needle concentration). This was followed by a second injection at the four-cell stage of 5 nL of p115.S wobble and/or fluorescently tagged probes. Injected embryos were placed at 15°C for ~24 h until they reached gastrulation (Nieuwkoop and Faber stages 10–11). The amount of mRNA per 5 nL microinjection volume was as follows: p115.S-mNeon, 13 pg (for live imaging) or 146 pg (for

embryo lysate preparation); p115.L-mNeon, 13 pg; p115.S wobble-mNeon, 146 pg (1× OE, for embryo lysate preparation) and 292 pg (2× OE, for embryo lysate preparation); untagged p115.S wobble, 78 pg; LARG.L-mNeon, 12 pg; PDZRhoGEF.S-mNeon, 18 pg, p114.S-mNeon, 55 pg; mCherry-2xrGBD, 66 pg; BFP-ZO-1, 50 pg; GFP-occludin, 8 pg; mCherry-occludin, 8 pg; mCherry-H2B, 25 pg.

### Embryo lysates and immunoblotting

Gastrula-stage embryos (Nieuwkoop and Faber stages 10–11) were lysed as previously described (Reyes *et al.*, 2014). Samples were separated on 4–20% Mini-PROTEAN TGX precast gels (Bio-Rad, #4561094) and transferred to nitrocellulose membranes. Membranes were blocked in 1× Tris-buffered saline (20 mM Tris and 150 mM NaCl) and 0.1% TWEEN-20, pH 7.6 (TBST), with 5% nonfat dry milk. Membranes were probed with anti-mNeon (1:100) or anti-α-tubulin (1:2500) antibodies overnight at 4°C in TBST with 3% nonfat dry milk. Membranes were washed three times (15 min each) with TBST. HRP (horseradish peroxidase) -conjugated secondary antibodies were applied at a concentration of 1:5000 in TBST with 3% nonfat dry milk and incubated for 1 h at room temperature (RT). Membranes were washed three times (15 min each) in TBST. Membranes were developed using an ECL detection kit (Fisher, #32209). Blots were imaged using the LI-COR Odyssey XF imaging system, with a 10-min exposure for anti-mNeon and a 2-min exposure for anti-α-tubulin.

### Antibodies

The primary antibodies used for Western blotting were anti-mNeon (Chromotek, #32f6) and anti-α-tubulin (Sigma, T9026). The secondary antibody used for Western blotting was HRP–conjugated anti-mouse (Fisher, #PRW4021). The primary antibodies used for immunofluorescence staining were as follows: anti-Phospho-myosin II Light Chain 2 (P-MLC; Cell Signaling Technology, #3671), anti-ZO-1 (Invitrogen, #61-7300), and anti-E-cadherin (Developmental Studies Hybridoma Bank, #5D3-C). The secondary antibodies used for immunofluorescence staining were as follows: anti-rabbit-Alexa Fluor 647 (Invitrogen, #A-21244), anti-rabbit-Alexa Fluor 568 (Invitrogen, #A-11011), and anti-mouse-Alexa Fluor 568 (Invitrogen, #A-11004).

### Immunofluorescence staining

***F-actin (phalloidin) and P-MLC.*** Albino embryos were injected with control (water), 2 mM of p115.S+L MOs, 2 mM p115.S MO, or 2 mM p115.S MO and untagged p115.S wobble. Embryos were fixed at the gastrula stage with paraformaldehyde (PFA) as previously described (Arnold *et al.*, 2019). Briefly, embryos were fixed overnight at RT with a mixture of 1.5% PFA, 0.25% glutaraldehyde, 0.2% Triton X-100, and either Alexa Fluor 647 phalloidin (1:100, Thermo Scientific, #A22287) or Alexa Fluor 488 phalloidin (1:100, Thermo Scientific, #A12379) in 0.88× MT buffer (80 mM K-Pipes, 5 mM EGTA, and 1 mM $MgCl_2$, adjusted to pH 6.8 with KOH). Fixed embryos were washed three times with 1× phosphate-buffered saline (PBS), quenched for 1 h at RT with 100 mM sodium borohydride in 1× PBS, washed again one time with 1× PBS, and bisected with a sharp scalpel to remove the vegetal hemisphere. Animal caps of the bisected embryos were blocked overnight in blocking solution (10% fetal bovine serum [FBS], 5% DMSO, and 0.1% NP-40 in 1× Tris-buffered saline). After blocking, animal caps were incubated overnight at 4°C in anti-P-MLC antibody (1:100) in blocking solution, washed three times (5 min, 15 min, and then 2 h) with blocking solution, and incubated overnight at 4°C in either anti-rabbit Alexa Fluor 568 (1:2000) and Alexa Fluor 647 phalloidin (1:85) or anti-rabbit Alexa Fluor 647 (1:2000) and Alexa Fluor 488 phalloidin (1:85) in blocking solution. Animal caps were washed and mounted in 1× PBS before imaging.

***ZO-1 and E-cadherin.*** Albino embryos were injected with control (water), 2 mM p115.S+L MOs, 2 mM p115.S MO, or 2 mM p115.S MO and untagged p115.S wobble. Embryos were fixed at gastrula stage with TCA as previously described (Reyes *et al.*, 2014). Briefly, embryos were fixed for 2 h at RT in 2% TCA in PBS. Fixed embryos were washed three times with 1× PBS and bisected with a sharp scalpel to remove the vegetal hemisphere. Animal caps of the bisected embryos were permeabilized for 20 min at RT in 1% Triton X-100 in 1× PBS, followed by a 20 min incubation in 1× PBST (0.1% Triton X-100 in 1× PBS). Permeabilized animal caps were blocked overnight at 4°C in blocking solution (5% FBS in 1 × PBST). After blocking, animal caps were incubated overnight at 4°C in anti-E-cadherin (1:1000) and anti-ZO-1 (1:200) antibodies in blocking solution. After three washes (5 min, 15 min, and then 2 h) in blocking solution animal caps were incubated for 6 h at 4°C in anti-mouse Alexa Fluor 568 (1:200) and anti-rabbit Alexa Fluor 647 (1:200) in blocking solution. Animal caps were washed and mounted in 1× PBS before imaging.

### Microscopy

***Live imaging.*** Live imaging of gastrula-stage *Xenopus* embryos was performed on an inverted Olympus FluoView 1000 microscope equipped with a 60× supercorrected Plan Apo N 60× OSC objective (NA = 1.4, working distance = 0.12 mm) using mFV10-ASW software. Embryos were mounted for imaging as previously described (Reyes *et al.*, 2014). Initial live imaging of mNeon-tagged candidate rgRGS GEFs, BFP-ZO-1, and mCherry-2xrGBD (active Rho probe) was captured with 8 apical Z-planes (step size 0.5 µm) acquired sequentially by line to avoid bleed through between channels. The scan speed was 4 µs/pixel with a 28s time interval at a 1.5× zoom. p115.S-mNeon, BFP-ZO-1, and Rho flare movies were acquired using the 3 apical Z-planes at a 2 µs/pixel scan speed, 7 s time interval at a 1.5× zoom. p115.S MO, GFP-occludin, and Rho flare movies were acquired with the same parameters described for p115.S-mNeon. Multicell view images of BFP-ZO-1 and p115.S-mNeon were captured by scanning the first 35 apical Z-planes at a 4 µs/pixel scan speed and 3.0× zoom. Mosaic images of p115.S+L MOs, p115.S MO, GFP-occludin, and active RhoA were captured by scanning 10 apical Z-planes with a 2 µs/pixel scan speed and a 1.5× zoom. Cell view images of active RhoA and p115RhoGEF MOs were captured by scanning the first 10 apical Z-planes at a 2 µs/pixel scan speed and 1.5× zoom. Cell view images of GFP-occludin and mCherry-H2B were captured by scanning the first 40 apical Z-planes at a 2 µs/pixel scan speed and 1.5× zoom.

***Fixed imaging.*** Bisected albino embryos were transferred into 1× PBS and mounted with the animal cap facing up within a small vacuum grease circle on a glass slide. A glass coverslip was placed over the animal cap and gently pressed down to flatten the bisected embryo. Images of embryos stained with phalloidin, P-MLC, anti-ZO-1, and anti-E-cadherin were acquired using the 30–35 Z-planes from the apical surface with a 12.5 µs/pixel scanning speed and a 1.5× zoom.

***Live imaging barrier assay.*** ZnUMBA was performed as previously reported (Stephenson *et al.*, 2019) with the following modifications: gastrula-stage albino embryos expressing mCherry-occludin (control) or mCherry-occludin and p115.S MO (p115.S KD) were microinjected into the blastocoel with 10 nL of 1 mM FluoZin-3 containing 100 µM $CaCl_2$ and 100 µM EDTA. Embryos were allowed to recover for 1 h at 15°C in 0.1× MMR. Following recovery, embryos were mounted in 0.1× MMR containing 1 mM $ZnCl_2$ and imaged immediately using confocal microscopy using the following acquisition

parameters: 8 apical Z-planes were acquired at a 4 µs/pixel scanning speed, 28s time interval at a 1.5× zoom.

***Images of Xenopus embryos at different developmental stages.*** Images of *X. laevis* embryos injected with control (water), 2 mM p115.S+L MOs, 2 mM p115.S MO, or 2 mM p115.S MO + p115.S wobble were captured with an Olympus SZX7-TR30 stereoscope using the Olympus EP50 camera and EPview app. The zoom was set to 2× for all stages except for stages 26 and 34, which required a zoom of 1.5×. Embryos were kept in a 15°C incubator during development and only removed for imaging.

### Image processing and quantification

Image processing and analysis were performed using Image J (FIJI). Sum intensity projections of the Z-stack were used for all quantification. Raw data were used for all quantification. For data presentation, LUTs were applied and scaled as described in the figure legends. Confocal images from time-lapse movies represented in the figures are sum projections of 3 apical Z-planes (1.5 µm total depth), except for a multicell view of active RhoA (10 apical Z-planes, 5 µm total depth), a multicell view of BFP-ZO-1 and p115.S-mNeon (35 apical Z-planes, 17.5 µm total depth), a multicell view of GFP-occludin and mCherry-H2B (40 apical Z-planes, 20 µm total depth), and FluoZin-3 (8 apical Z-planes, 4 µm total depth). Fixed images of phalloidin, P-MLC, ZO-1, and E-cadherin are sum projections of 30 apical Z-planes (15 µm total depth).

***Quantification of p115RhoGEF dynamics during Rho flares.*** Quantification of the intensity of p115RhoGEF-mNeon, BFP-ZO-1, GFP-occludin, and active Rho probe (mCherry-2xrGBD) over time in control and knockdown experiments was performed as previously reported (Stephenson *et al.*, 2019; Varadarajan *et al.*, 2022) with the following modification: the small circular region of interest (ROI) had a diameter of 0.69 µm.

***Side-view projections of ZO-1 and p115.S.*** Side-view projections of BFP-ZO-1 and p115.S-mNeon were acquired by capturing 35 apical Z-planes. The Z-stack was opened in FIJI and was not sum projected. First, a horizontal, 0.5 µm-wide segmented line was drawn perpendicular to several bicellular junctions (see white dashed line in Supplemental Figure S1D). The 3D projection tool in FIJI was then used to generate a side-view image. Second, a rectangular ROI was drawn encompassing an individual bicellular junction, not including the vertices (see yellow dashed box in Supplemental Figure S1D). The 3D projection tool was used to generate a side view along the plane of the membrane.

***Area under the curve for Rho flares.*** Area under the curve (AUC) for active Rho flares was quantified using GraphPad Prism 9.0 by AUC analysis of the individual Rho flare traces. AUC analysis was applied to all points in the peaks above the baseline of 1; peaks less than 10% of the increase from the baseline to the maximum Y value were excluded. Individual AUC values for each Rho flare for control and p115RhoGEF knockdown were plotted in a scatter plot.

***Junction length measurements.*** Junction length was quantified using occludin as a junctional marker. Using FIJI, a 0.3-µm-wide segmented line was drawn on junctions with Rho flares from vertex-to-vertex every 10 frames and saved into the ROI manager. The time-lapse and line of interest interpolator plug-in then generated an ROI for each frame of the time-lapse movie, accommodating for cell shape changes. Each junction was measured in triplicate, and change in length was calculated by subtracting the individual values from the average of the first 65 s.

***Construction of kymographs.*** Kymographs from vertex-to-vertex of a cell–cell junction were constructed using occludin as a junctional marker. In FIJI, a 0.5-µm-wide segmented line was drawn on junctions every 10 frames and saved into the ROI manager (a total of 200 frames for Figure 2 and 50 frames for Figure 4). The time-lapse and LOI interpolator plug-in then generated an ROI for each frame of the time-lapse movie, accommodating for cell shape changes, and created a kymograph of those ROIs over time.

***Frequency of Rho flares.*** Rho flare frequency was measured manually using FIJI by counting the number of Rho flare occurrences at cell–cell junctions in the whole field of imaging from the start of the time-lapse movie to the end (a total of 15 min for each movie). Frequency was reported in graphs as flares/minute. Rho flares where the local active RhoA intensity increased and was sustained at the junctions for a span of ~80–100s were included in the analysis.

***Apical cell surface area measurements.*** Apical cell surface area was measured using GFP-occludin. For all images, we used sum projections of 10 apical Z-slices. Some images did not have sufficient signal for automated quantification; in those cases, cells were outlined by hand using the polygon selection tool in FIJI (4 of 20 images). For all other images, cell surface area was quantified as follows using FIJI. The image was duplicated to create two copies (Images A and B). A Gaussian blur with a radius of 15 was applied to Image B to remove noise. Using the image calculator, Image B was subtracted from Image A to create Image C. A Gaussian blur with a radius of 3 was applied to Image C to detect continuous junctions. Then, thresholding was applied to Image C by manually adjusting the minimum and maximum cutoffs to maximize junction continuity. The signal was then dilated until all junctions were continuous. Then Image C was skeletonized, the signal was dilated one time, and the image was inverted. The area was measured using Analyze Particles where the size was limited from 20 to infinity microns, and cells along the edge of the image were excluded.

***Intensity of F-actin (phalloidin), P-MLC, ZO-1, and E-cadherin.*** The junction/cytoplasm intensity ratios for F-actin (phalloidin), P-MLC, ZO-1, and E-cadherin were quantified in FIJI. Junctional intensity was measured with a 0.3-µm-wide segmented line along bicellular junctions (excluding vertices), and cytoplasmic intensity was measured using a 10.14-µm-circular ROI. For each image, we measured five junctions, which were averaged constituting one data point. The ratio of junctional/cytoplasmic intensity of F-actin (phalloidin), P-MLC, ZO-1, and E-cadherin was calculated by dividing the average intensity at the junction by the average intensity in the cytoplasm for each image.

### Whole-field FluoZin-3 intensity

Whole-field FluoZin-3 intensity was quantified as previously reported (Varadarajan *et al.*, 2022) with the following modification: the baseline was normalized to 1 by dividing each individual value by the average of the first 83 s.

### Statistical analysis

Unpaired Student's *t* tests were used to determine the statistical significance of each group pairwise between control and p115.S+L KD, p115.S KD, or p115.S KD + p115.S wobble. Statistics were calculated in GraphPad Prism 9.0 software.

## ACKNOWLEDGMENTS

We thank all current and former members of the A.L.M. laboratory for providing helpful discussion and feedback on the manuscript, especially Jennifer Landino for providing experimental advice and edits on the manuscript and Rachel Stephenson for advice on Rho flare analysis, ZnUMBA, and kymograph construction. We thank Akash Rai for assistance with cloning and initial imaging of p115.S-mNeon. This work was supported by an NIH Grant (2R01 GM112794) to A.L.M., an NSF Graduate Research Fellowship to S.A.C., and a predoctoral fellowship from the American Heart Association (906189) to L.M.v.d.G.

## REFERENCES

Acharya BR, Nestor-Bergmann A, Liang X, Gupta S, Duszyc K, Gauquelin E, Gomez GA, Budnar S, Marcq P, Jensen OE, *et al.* (2018). A mechanosensitive RhoA pathway that protects epithelia against acute tensile stress. Dev Cell 47, 439–452.e436.

Arnold TR, Shawky JH, Stephenson RE, Dinshaw KM, Higashi T, Huq F, Davidson LA, Miller AL (2019). Anillin regulates epithelial cell mechanics by structuring the medial-apical actomyosin network. Elife 8, e39065.

Arnold TR, Stephenson RE, Miller AL (2017). Rho GTPases and actomyosin: Partners in regulating epithelial cell-cell junction structure and function. Exp Cell Res 358, 20–30.

Benais-Pont G, Punn A, Flores-Maldonado C, Eckert J, Raposo G, Fleming TP, Cereijido M, Balda MS, Matter K (2003). Identification of a tight junction-associated guanine nucleotide exchange factor that activates Rho and regulates paracellular permeability. J Cell Biol 160, 729–740.

Benink HA, Bement WM (2005). Concentric zones of active RhoA and Cdc42 around single cell wounds. J Cell Biol 168, 429–439.

Birkenfeld J, Nalbant P, Bohl BP, Pertz O, Hahn KM, Bokoch GM (2007). GEF-H1 modulates localized RhoA activation during cytokinesis under the control of mitotic kinases. Dev Cell 12, 699–712.

Breznau EB, Semack AC, Higashi T, Miller AL (2015). MgcRacGAP restricts active RhoA at the cytokinetic furrow and both RhoA and Rac1 at cell-cell junctions in epithelial cells. Mol Biol Cell 26, 2439–2455.

Cavanaugh KE, Staddon MF, Munro E, Banerjee S, Gardel ML (2020). RhoA mediates epithelial cell shape changes via mechanosensitive endocytosis. Dev Cell 52, 152–166.e155.

Citi S, Spadaro D, Schneider Y, Stutz J, Pulimeno P (2011). Regulation of small GTPases at epithelial cell-cell junctions. Mol Membr Biol 28, 427–444.

Davenport NR, Sonnemann KJ, Eliceiri KW, Bement WM (2016). Membrane dynamics during cellular wound repair. Mol Biol Cell 27, 2272–2285.

Dubash AD, Wennerberg K, Garcia-Mata R, Menold MM, Arthur WT, Burridge K (2007). A novel role for Lsc/p115 RhoGEF and LARG in regulating RhoA activity downstream of adhesion to fibronectin. J Cell Sci 120, 3989–3998.

Duszyc K, Gomez GA, Lagendijk AK, Yau MK, Nanavati BN, Gliddon BL, Hall TE, Verma S, Hogan BM, Pitson SM, *et al.* (2021). Mechanotransduction activates RhoA in the neighbors of apoptotic epithelial cells to engage apical extrusion. Curr Biol 31, 1326–1336.e1325.

Fritz RD, Pertz O (2016). The dynamics of spatio-temporal Rho GTPase signaling: formation of signaling patterns. F1000Res 5.

Fukuhara S, Chikumi H, Gutkind JS (2001). RGS-containing RhoGEFs: the missing link between transforming G proteins and Rho? Oncogene 20, 1661–1668.

Garcia De Las Bayonas A, Philippe JM, Lellouch AC, Lecuit T (2019). Distinct RhoGEFs activate apical and junctional contractility under control of G proteins during epithelial morphogenesis. Curr Biol 29, 3370–3385 e3377.

Garcia-Mata R, Burridge K (2007). Catching a GEF by its tail. Trends Cell Biol 17, 36–43.

Gudipaty SA, Rosenblatt J (2017). Epithelial cell extrusion: Pathways and pathologies. Semin Cell Dev Biol 67, 132–140.

Guillot C, Lecuit T (2013). Mechanics of epithelial tissue homeostasis and morphogenesis. Science 340, 1185–1189.

Hartsock A, Nelson WJ (2008). Adherens and tight junctions: structure, function and connections to the actin cytoskeleton. Biochim Biophys Acta 1778, 660–669.

Higashi T, Arnold TR, Stephenson RE, Dinshaw KM, Miller AL (2016). Maintenance of the epithelial barrier and remodeling of cell-cell junctions during cytokinesis. Curr Biol 26, 1829–1842.

Holinstat M, Mehta D, Kozasa T, Minshall RD, Malik AB (2003). Protein kinase Calpha-induced p115RhoGEF phosphorylation signals endothelial cytoskeletal rearrangement. J Biol Chem 278, 28793–28798.

Huang C, Liu S, Miller RT (2011). Role of p115RhoGEF in the regulation of extracellular Ca(2+)-induced choline kinase activation and prostate cancer cell proliferation. Int J Cancer 128, 2833–2842.

Huebner RJ, Wallingford JB (2019). Coming to Consensus: A Unifying Model Emerges for Convergent Extension. Dev Cell 48, 126.

Ivanov AI, Parkos CA, Nusrat A (2010). Cytoskeletal regulation of epithelial barrier function during inflammation. Am J Pathol 177, 512–524.

Kher SS, Struckhoff AP, Alberts AS, Worthylake RA (2014). A novel role for p115RhoGEF in regulation of epithelial plasticity. PLoS One 9, e85409.

Kozasa T, Jiang X, Hart MJ, Sternweis PM, Singer WD, Gilman AG, Bollag G, Sternweis PC (1998). p115 RhoGEF, a GTPase activating protein for Galpha12 and Galpha13. Science 280, 2109–2111.

Marchiando AM, Graham WV, Turner JR (2010). Epithelial barriers in homeostasis and disease. Annu Rev Pathol 5, 119–144.

Martin JW, Cavagnini KS, Brawley DN, Berkley CY, Smolski WC, Garcia RD, Towne AL, Sims JR, Meigs TE (2016). A Galpha12-specific binding domain in AKAP-Lbc and p114RhoGEF. J Mol Signal 11, 3.

Miller AL, Bement WM (2009). Regulation of cytokinesis by Rho GTPase flux. Nat Cell Biol 11, 71–77.

Moruzzi M, Nestor-Bergmann A, Goddard GK, Tarannum N, Brennan K, Woolner S (2021). Generation of anisotropic strain dysregulates wild-type cell division at the interface between host and oncogenic tissue. Curr Biol 31, 3409–3418.e3406.

Priya R, Gomez GA, Budnar S, Verma S, Cox HL, Hamilton NA, Yap AS (2015). Feedback regulation through myosin II confers robustness on RhoA signalling at E-cadherin junctions. Nat Cell Biol 17, 1282–1293.

Reyes CC, Jin M, Breznau EB, Espino R, Delgado-Gonzalo R, Goryachev AB, Miller AL (2014). Anillin regulates cell-cell junction integrity by organizing junctional accumulation of Rho-GTP and actomyosin. Curr Biol 24, 1263–1270.

Rosenblatt J, Raff MC, Cramer LP (2001). An epithelial cell destined for apoptosis signals its neighbors to extrude it by an actin- and myosin-dependent mechanism. Curr Biol 11, 1847–1857.

Rossman KL, Der CJ, Sondek J (2005). GEF means go: turning on RHO GTPases with guanine nucleotide-exchange factors. Nat Rev Mol Cell Biol 6, 167–180.

Saito AC, Higashi T, Fukazawa Y, Otani T, Tauchi M, Higashi AY, Furuse M, Chiba H (2021). Occludin and tricellulin facilitate formation of anastomosing tight-junction strand network to improve barrier function. Mol Biol Cell 32, 722–738.

Scott DW, Tolbert CE, Burridge K (2016). Tension on JAM-A activates RhoA via GEF-H1 and p115 RhoGEF. Mol Biol Cell 27, 1420–1430.

Session AM, Uno Y, Kwon T, Chapman JA, Toyoda A, Takahashi S, Fukui A, Hikosaka A, Suzuki A, Kondo M, *et al.* (2016). Genome evolution in the allotetraploid frog Xenopus laevis. Nature 538, 336–343.

Stephenson RE, Higashi T, Erofeev IS, Arnold TR, Leda M, Goryachev AB, Miller AL (2019). Rho flares repair local tight junction leaks. Dev Cell 48, 445–459.e445.

Storch U, Mederos y Schnitzler M, Gudermann T (2012). G protein-mediated stretch reception. Am J Physiol Heart Circ Physiol 302, H1241–1249.

Terry SJ, Zihni C, Elbediwy A, Vitiello E, Leefa Chong San IV, Balda MS, Matter K (2011). Spatially restricted activation of RhoA signalling at epithelial junctions by p114RhoGEF drives junction formation and morphogenesis. Nat Cell Biol 13, 159–166.

Thumkeo D, Watanabe S, Narumiya S (2013). Physiological roles of Rho and Rho effectors in mammals. Eur J Cell Biol 92, 303–315.

Turner JR (2000). 'Putting the squeeze' on the tight junction: understanding cytoskeletal regulation. Semin Cell Dev Biol 11, 301–308.

Van Itallie CM, Tietgens AJ, Anderson JM (2017). Visualizing the dynamic coupling of claudin strands to the actin cytoskeleton through ZO-1. Mol Biol Cell 28, 524–534.

Varadarajan S, Chumki SA, Stephenson RE, Misterovich ER, Wu JL, Dudley CE, Erofeev IS, Goryachev AB, Miller AL (2022). Mechanosensitive calcium flashes promote sustained RhoA activation during tight junction remodeling. Journal of Cell Biology 221, e202105107.

Varadarajan S, Stephenson RE, Miller AL (2019). Multiscale dynamics of tight junction remodeling. J Cell Sci 132, jcs229286.

Vizurraga A, Adhikari R, Yeung J, Yu M, Tall GG (2020). Mechanisms of adhesion G protein-coupled receptor activation. J Biol Chem 295, 14065–14083.

Woolner S, Miller AL, Bement WM (2009). Imaging the cytoskeleton in live Xenopus laevis embryos. Methods Mol Biol 586, 23–39.

Yuce O, Piekny A, Glotzer M (2005). An ECT2-centralspindlin complex regulates the localization and function of RhoA. J Cell Biol 170, 571–582.

Zeissig S, Burgel N, Gunzel D, Richter J, Mankertz J, Wahnschaffe U, Kroesen AJ, Zeitz M, Fromm M, Schulzke JD (2007). Changes in expression and distribution of claudin 2, 5 and 8 lead to discontinuous tight junctions and barrier dysfunction in active Crohn's disease. Gut 56, 61–72.